Bose, S, Dong, S, Elias-Rosa, N, Shappee, BJ, Bersier, D, Benetti, S, Stritzinger, MD, Grupe, D, Kochanek, CS, Prieto, JL, Chen, P, Kuncarayakti, H, Mattila, S, Morales-Garoffolo, A, Morrell, N, Onori, F, Reynolds, TM, Siviero, A, Somero, A, Stanek, KZ, Terreran, G, Thompson, TA, Tomasella, L, Ashall, C, Gall, C, Gromadzki, M and Holoien, TW-S

Strongly Bipolar Inner Ejecta of the Normal Type IIP Supernova ASASSN-16at

Draft version March 5, 2019
Typeset using LaTeX **twocolumn** style in AASTeX61

STRONGLY BIPOLAR INNER EJECTA OF THE NORMAL TYPE IIP SUPERNOVA ASASSN-16at

Subhash Bose,[1] Subo Dong,[1] N. Elias-Rosa,[2,3] B. J. Shappee,[4] David Bersier,[5] Stefano Benetti,[6] M. D. Stritzinger,[7] D. Grupe,[8] C. S. Kochanek,[9,10] J. L. Prieto,[11,12] Ping Chen,[1] H. Kuncarayakti,[13,14] Seppo Mattila,[14] Antonia Morales-Garoffolo,[15] Nidia Morrell,[16] F. Onori,[17] Thomas M Reynolds,[14] A. Siviero,[18] Auni Somero,[14] K. Z. Stanek,[9,10] Giacomo Terreran,[19] Todd A. Thompson,[9,10,20] L. Tomasella,[6] C. Ashall,[21] Christa Gall,[22] M. Gromadzki,[23] and T. W.-S. Holoien[24]

[1] *Kavli Institute for Astronomy and Astrophysics, Peking University, Yi He Yuan Road 5, Hai Dian District, Beijing 100871, China.*
[2] *Institute of Space Sciences (ICE, CSIC), Campus UAB, Carrer de Can Magrans s/n, 08193 Barcelona, Spain*
[3] *Institut dEstudis Espacials de Catalunya (IEEC), c/Gran Capitá 2-4, Edif. Nexus 201, 08034 Barcelona, Spain*
[4] *Institute for Astronomy, University of Hawaii, 2680 Woodlawn Drive, Honolulu, HI 96822, USA*
[5] *Astrophysics Research Institute, Liverpool Science Park, 146 Brownlow Hill, Liverpool L3 5RF, UK 0000-0001-7485-3020*
[6] *INAF-Osservatorio Astronomico di Padova, Vicolo dell'Osservatorio 5, I-35122 Padova, Italy*
[7] *Department of Physics and Astronomy, Aarhus University, Ny Munkegade 120, DK-8000 Aarhus C, Denmark*
[8] *Department of Earth and Space Sciences, Morehead State University, Morehead, KY, 40351, USA*
[9] *Department of Astronomy, The Ohio State University, 140 W. 18th Avenue, Columbus, OH 43210, USA.*
[10] *Center for Cosmology and AstroParticle Physics (CCAPP), The Ohio State University, 191 W. Woodruff Avenue, Columbus, OH 43210, USA.*
[11] *Núcleo de Astronomía de la Facultad de Ingeniería y Ciencias, Universidad Diego Portales, Av. Ej ército 441, Santiago, Chile*
[12] *Millennium Institute of Astrophysics, Santiago, Chile.*
[13] *Finnish Centre for Astronomy with ESO (FINCA), FI-20014 University of Turku, Finland.*
[14] *Tuorla Observatory, Department of Physics and Astronomy, FI-20014 University of Turku, Finland*
[15] *Department of Applied Physics, University of Cádiz, Campus of Puerto Real, E-11510 Cádiz, Spain*
[16] *Carnegie Observatories, Las Campanas Observatory, Casilla 601, La Serena, Chile*
[17] *Istituto di Astrofisica e Planetologia Spaziali, via Fosso del Cavaliere 100,I-00133 Rome, Italy*
[18] *Dipartimento di Fisica e Astronomia, Universit'a di Padova, via Marzolo 8, I-35131 Padova, Italy*
[19] *Center for Interdisciplinary Exploration and Research in Astrophysics (CIERA) and Department of Physics and Astronomy, Northwestern University, Evanston, IL 60208*
[20] *Institute for Advanced Study, 1 Einstein Dr, Princeton, New Jersey 08540*
[21] *Department of Physics, Florida State University, Tallahassee, FL 32306, USA*
[22] *Dark Cosmology Centre, Niels Bohr Institute, University of Copenhagen, Juliane Maries Vej 30, 2100 Copenhagen, Denmark*
[23] *Warsaw University Astronomical Observatory, Al. Ujazdowskie 4, 00-478 Warszawa, Poland*
[24] *Carnegie Observatories, 813 Santa Barbara Street, Pasadena, CA 91101, USA*

ABSTRACT

We report distinctly double-peaked $H\alpha$ and $H\beta$ emission lines in the late-time, nebular-phase spectra ($\gtrsim 200$ days) of the otherwise normal at early phases ($\lesssim 100$ days) Type IIP supernova ASASSN-16at (SN 2016X). Such distinctly double-peaked nebular Balmer lines have never been observed for a Type II SN. The nebular-phase Balmer emission is driven by the radioactive ^{56}Co decay, so the observed line-profile bifurcation suggests a strong bipolarity in the ^{56}Ni distribution or in the line-forming region of the inner ejecta. The strongly bifurcated blue- and red-shifted peaks are separated by $\sim 3 \times 10^3\,\mathrm{km\,s^{-1}}$ and are roughly symmetrically positioned with respect to the host-galaxy rest frame, implying that the inner ejecta are composed of two almost detached blobs. The red peak progressively weakens relative to the blue peak, and disappears in the 740 days spectrum. One possible reason for the line-ratio evolution

Corresponding author: Subo Dong, Subhash Bose
dongsubo@pku.edu.cn, email@subhashbose.com

is increasing differential extinction from continuous formation of dust within the envelope, which is also supported by the near-infrared flux excess that develops after ~ 100 days.

Keywords: supernovae: general − supernovae: individual: (ASASSN-16at, SN 2016X) − galaxies: individual: UGC 08041

1. INTRODUCTION

Hydrogen-rich, core-collapse supernovae (CCSNe), also known as type II SNe, originate from massive stars ($M \geq 8 M_{\odot}$) which have retained most of their hydrogen content at the time of explosion. From spectropolarimetry studies, CCSNe ejecta are often found to show a significant degree of asymmetry (see, e.g., the review by Wang & Wheeler 2008). In the early photospheric phase of SNe II, the inner ejecta is mostly obscured by the thick and extended envelope of ionized hydrogen, which become increasingly transparent as the ejecta expands and the hydrogen recombines. The late-time, "nebular phase" observations are particularly important to unveil the structure of the inner regions once the ejecta becomes optically thin. During the late-time ($\gtrsim 100 - 150$ d) light-curve tail, the optical radiation is primarily powered by the decay of radioactive ^{56}Co (the decay product of ^{56}Ni synthesized in the explosion), and the ^{56}Ni distribution in the ejecta can be reflected in the nebular Balmer emission line profiles (Chugai 2007), which can be a powerful probe of the explosion asymmetry. Despite decades of studies of SNe II, the exact mechanism driving the shock within the SN during the explosion is still under debate (see, e.g., Janka 2012; Pejcha & Thompson 2015; Kushnir & Katz 2015, and references therein), and non-sphericity and jets are often suspected to be critical to these explosions (e.g., Khokhlov et al. 1999; Janka 2012; Piran et al. 2017; Soker 2018). Studying the asymmetry of the ejecta, especially the inner region, may provide important clues in understanding the explosion mechanism.

CCSNe may be an important source of dust in the universe (see, e.g., Gall et al. 2011). During the nebular phase, as the ejecta cools, the gas may start to condense into dust grains and thereby increase the extinction locally. Dust formation has been observed in several CCSNe (e.g., Sugerman et al. 2006; Mattila et al. 2008; Kotak et al. 2009; Meikle et al. 2011; Inserra et al. 2011; Stritzinger et al. 2012; Maeda et al. 2013). The effect of newly formed dust can be manifested in the light curves and spectra of the SN. The dust absorbs the light and re-emits in infra-red (IR) resulting in strong IR excess. Substantial dust formation may also lead to asymmetries in nebular emission lines due to differential extinction as the light coming from the far side of the ejecta suffers more extinction.

Here we present detailed observations of the normal type IIP SN ASASSN-16at until its late nebular phase (up to $\sim$ 900 days). ASASSN-16at shows a unique double-peaked profile in Hα and Hβ nebular emission lines, where the relative strengths of the two peaks evolve with time. Such a distinct double-peaked structure is unprecedented for an SN IIP. Huang et al. (2018) studied the NUV-optical light curves and optical spectra of ASASSN-16at until the early radioactive decay tail phase, showing key features that are typical for a SN IIP. They also reported that, the Hα emission profile showed weak asymmetry in their last spectrum at 142d, for which they suggested three possible interpretations – circumstellar medium (CSM) interaction, asymmetry in the line-emitting region or bipolar ^{56}Ni distribution. Our still later nebular-phase spectra taken at $\gtrsim 200$ d show Balmer lines with double-peaked profiles, which most likely suggest a bipolar distribution of the inner ejecta. Our work focuses on the nebular data, while our full photometry and spectroscopic data are given in the Appendix.

2. OBSERVATIONS

ASASSN-16at was discovered in the host galaxy UGC 08041 by the All-Sky Automated Survey for Supernovae (ASAS-SN; Shappee et al. 2014) on UT 2016-01-20.59 using the "Brutus" telescope in Haleakala, Hawaii (Bock et al. 2016; Holoien et al. 2017). The first ASAS-SN detection was at $V = 16.81 \pm 0.26$ mag on UT 2016-01-19.49, and the last non-detection was $V < 18$ mag on UT 2016-01-18.35. We adopt the explosion epoch of 2016-01-18.92 (JD 2457406.42 $\pm$ 0.57) and use this as the reference epoch throughout the paper. The host galaxy distance is 15.2 ± 3.0 Mpc according to Sorce et al. (Tully-Fisher distance; 2014). We ignore any host-galaxy extinction since we do not detect any Na I D absorption in the SN spectrum, which is consistent with the fairly isolated location of the SN in the outskirts of the host galaxy. We adopt a total line-of-sight reddening entirely due to Milky-Way of $E(B-V) = 0.019$ mag (Schlafly & Finkbeiner 2011) and $R_V = 3.1$.

We obtained near-ultraviolet (NUV) through near-infrared (NIR) photometry and optical spectroscopy of ASASSN-16at from 0.6d to 881d. The NUV observations were obtained with the Neil-Gehrels-Swift-Observatory UVOT. X-ray observations were obtained using the *Swift* XRT and *Chandra*. We summarize our optical photometric and spectroscopic observations in the Appendix, and the photometric results are reported in Table. 2, and logs of the spectroscopic observations are given in Table 3.

3. RESULTS

Optical spectra were obtained from 2d to a late nebular phase of 740 d. We find that the early-phase ($\lesssim 100$ d) spectroscopic properties of ASASSN-16at are typical for a normal SNe IIP, in agreement with Huang et al. (2018). However, the nebular spectra taken at

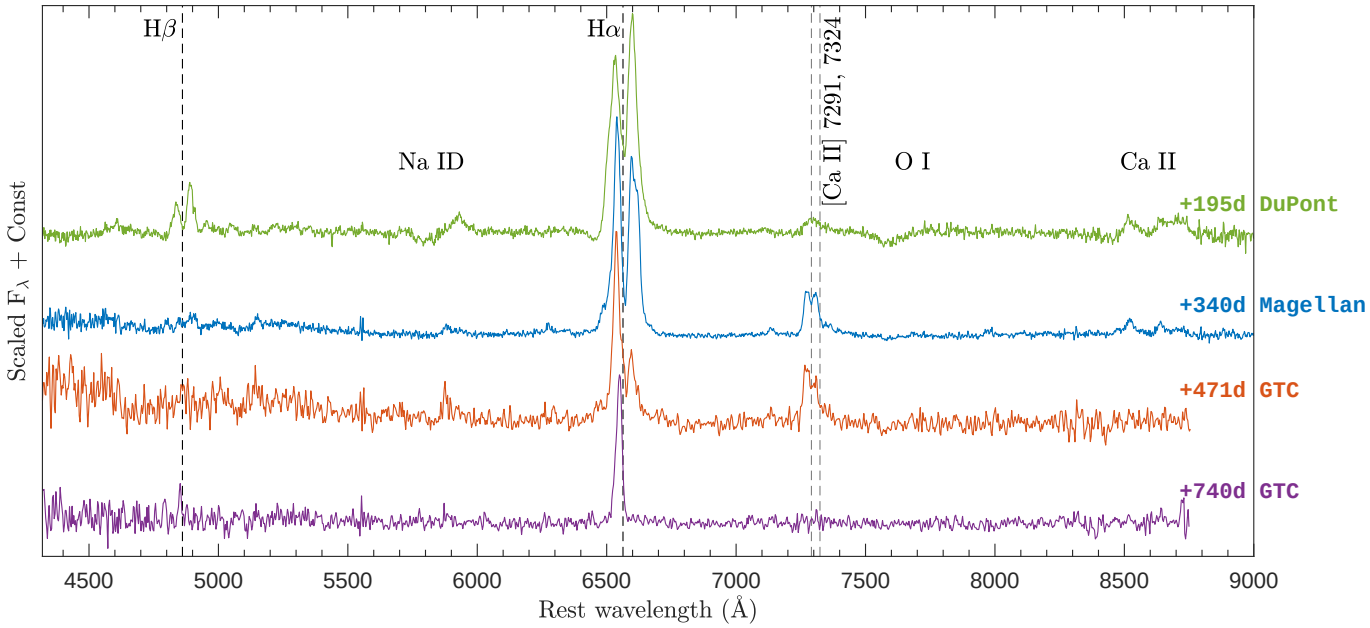

Figure 1. Deep nebular spectra of ASASSN-16at at 4 epochs (195 d, 340 d, 471 d and 740 d). The vertical dashed lines mark the rest wavelengths of the Hα, Hβ and the [Ca II] doublet.

$\gtrsim$ 200 d make this SN IIP exceptional. Fig. 1 shows the nebular phase spectra of ASASSN-16at at 195, 340, 471 and 740 d. Starting from 195 d, which is $\sim$ 100 days after the onset of the radioactive tail phase the Hα and Hβ emissions show a very unusual double-peaked profile, where the two peaks, separated by $\sim 3\times10^3$ km s^{-1}, are positioned almost symmetrically in velocity with respect to the rest frame of the host galaxy. Among the two components, the relative strength of the red component is seen to be progressively decreasing with time relative to the blue component (see Fig. 2). At 740d, the red component is no longer detectable, whereas the blue component of both Hα and Hβ remains visibly strong, albeit narrower and shifted closer to the rest frame than in the earlier spectra. See Table 1 in the Appendix for the parameters estimated from the Hα and Hβ line profiles. The Hα emission line is detected in all the nebular spectra, while Hβ is not clearly seen in the spectra taken at 340 and 471d, both of which have a relatively low signal-to-noise ratio. The other nebular lines detectable in these spectra are Na I D (λ5890), O I (λ7774), Ca II triplets ($\lambda\lambda$8498, 8542, 8062) and the strong emission of [Ca II] ($\lambda\lambda$7291, 7324).

The photometric light curves span from 0.6 d to 881 d and are shown in Fig. 3. Huang et al. (2018) presented NUV and optical light curves up to 170d, and our photometric measurements during this period are consistent with their results. The NUV, optical and NIR light curves show the typical evolution of SN IIP, except in the late nebular phase ($\gtrsim$ 500 d), where the light curves decline more slowly than the typical SNe IIP, especially in the g and r bands. The flux contamination from the host galaxy may not be entirely negligible at this very late phase, but our analysis using archival Pan-STARRS1 images (Chambers et al. 2016) suggests that the observed flattening is mostly intrinsic to the SN.

ASASSN-16at was observed in 0.3-10 keV using the *Swift* and *Chandra* X-ray telescopes during $2-18$ d (see Fig. 7 in Appendix). The X-ray luminosity during the initial phases of $2-5$ d is about 25×10^{38} erg s^{-1}, which is around the typical luminosity for SNe II with X-ray detections (see, e.g. Pooley et al. 2002; Dwarkadas & Gruszko 2012). However, the luminosity declined to 5×10^{38} erg s^{-1}by $\sim$ 19 d.

4. DISCUSSION

Some SNe II shows some level of asymmetry in their nebular Hα emission, and a bipolar or asymmetric distribution of radioactive ^{56}Ni in the inner ejecta has been invoked as a possible interpretation. Some notable SNe with nebular Hα asymmetries include SNe 1987A (Utrobin et al. 1995), 1999em (Elmhamdi et al. 2003), 2004dj (Chugai et al. 2005; Chugai 2006), 2012A (Tomasella et al. 2013) and 2013ej (Bose et al. 2015b; Utrobin & Chugai 2017). However, none of the SNe IIP observed to date have shown such a prominent bifurcation in nebular Hα and Hβ emissions as in ASASSN-16at, where each component of the double-peaked structure is distinctly resolved (see Fig. 4 for comparison). While there might be alternative scenarios such as self-absorption, we interpret this double-peaked profile to be most likely due to strong bipolarity in the

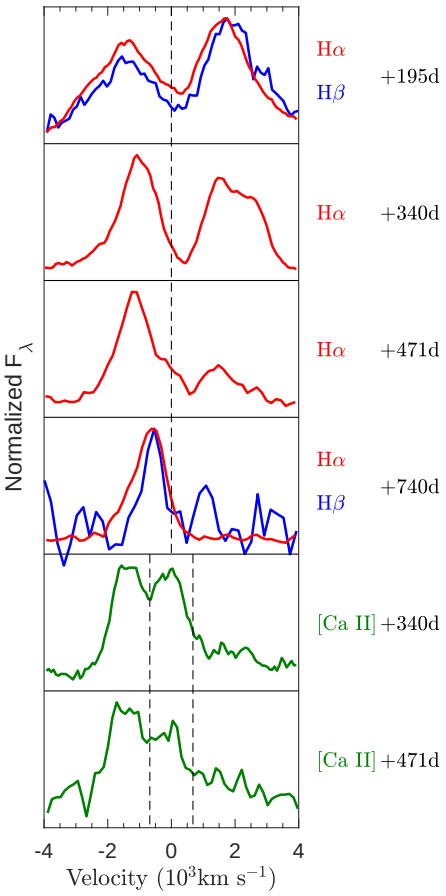

Figure 2. Hα Hβ and [Ca II] nebular lines shown in the velocity domain with respect to the rest wavelengths of Hα, Hβ and an average of [Ca II] doublet. The vertical dashed lines mark the positions of zero velocity for Hα Hβ and [Ca II] doublet.

^{56}Ni distribution or in the line-forming region within the inner ejecta. In SNe II, the radioactive ^{56}Ni is likely well mixed with the ejecta (e.g., Shigeyama & Nomoto 1990), so the bipolarity seen in the inner-ejecta may imply the bipolarity in the ^{56}Ni distribution. Alternatively, the line-forming region is bipolar. The prominent bifurcation of the line about the rest position likely suggests that the the inner ejecta is composed of a pair of almost-detached blobs.

An additional intriguing feature of the nebular H I emission seen in ASASSN-16at is the time evolution of its morphology. The red component of the Hα and Hβ emission progressively decreases in strength relative to the blue component. This evolution can be a direct consequence of differential extinction due to late-time dust formation in the inner ejecta. The red component is emitted from regions located on the far side of the ejecta while the blue component is emitted on the near side. Consequently, the redder component suffers more line-of-sight extinction as compared to the bluer component due to the dust formed within the ejecta. As more and more dust is formed with, the redder component suffers increasing extinction causing it to diminish in relative strength. Ultimately at 740d, the redder component is completely obscured, while the bluer component of Hα and Hβ is still well detected at ~ -600 km s^{-1}. The alternative scenario explaining the blue-to-red ratio evolution of the H I profile, which we view as less likely, is that the changes are intrinsic to the emitting regions of inner ejecta. However, the change in shape of the red-component among +195 d, +340 d and +471 d is likely intrinsic to emitting regions.

The effect of differential extinction due to dust is also consistent with the blue-skewed profiles of the [Ca II] doublet ($\lambda\lambda$ 7291, 7342) in the nebular spectra shown in Fig. 2. Because the [Ca II] emission feature is intrinsically a doublet, it is not straightforward to determine if it has a double-peaked profile. However, it is clear that the peaks of the doublets are shifted blue-ward with respect to the rest frame. From 340d to 471d, the redder component is similarly suppressed, though to a less degree, as we could see for the H I line evolution at the same epochs. This change in line profile may further support increasing dust extinction if we assume the profile is dominantly the double-peaked components of [Ca II], instead of just the resolved doublet. This is similar to what was observed in the [Ca II] nebular emission of SN 2007od (Inserra et al. 2011), which was also interpreted as a result of dust extinction in the ejecta.

To further examine dust formation, we investigate the K-band photometry. Ideally a quantitative comparison should be made with theoretical expectations, but robust calculations predicting NIR SED evolution for SNe II do not exist to our knowledge, thus we take an empirical approach by comparing with K-band observations of other SNe II. The top panel of Fig. 5 shows the evolution of the $(i-K)$ color, which becomes significantly redder between 102 d ($\sim$ 1.5 mag) and 735 d ($\sim$ 3.6 mag). Since Hα and Hβ line emission contribute strongly to the g and r-band fluxes, these bands are not used to evaluate the optical-to-NIR color or to construct the SED. For comparison, we also show the evolution of the $(i-K)$ color of SNe 1987A (Bouchet & Danziger 1993, and references therein), 2004dj (IIP; Meikle et al. 2011), 2004et (IIP; Maguire et al. 2010; Kotak et al. 2009), 2011dh (IIb; Ergon et al. 2015), which also had evidence of dust formation at late times based on their Mid-IR (MIR) observations with estimated dust masses of $M_{dust} \approx 10^{-4} - 10^{-3} M_\odot$ at similar phases. The optical-to-NIR color of ASASSN-16at is significantly redder than the comparison sample at all phases and shows an increasing trend in reddening, supporting late-

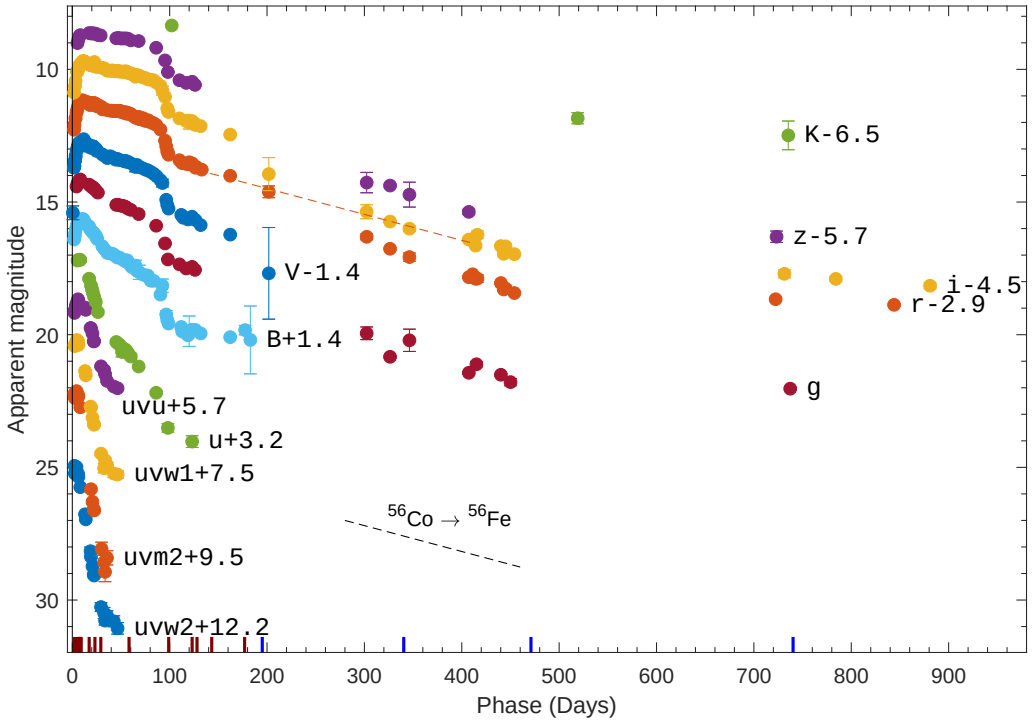

Figure 3. The photometric evolution of ASASSN-16at in the *Swift* NUV, optical $BVugriz$-bands and NIR K-band. Epochs of spectral observations are marked by vertical bars at the bottom, and the four nebular spectra showing double-peaked emission are marked in blue. Within $200-500$ days, all the light curves declined at a faster rate than radioactive ^{56}Co decay, which is illustrated only for the r band by a red dashed line representing ^{56}Co decay rate.

time dust formation in ASASSN-16at and possibly more than the comparison SNe. The SED (the bottom panel of Fig. 5) evolves from a peak in optical to peak toward IR, again supporting the formation of dust during this period. We note that the Hα to Hβ line ratios are 5.7 ± 0.7 at 195 d and 3.9 ± 1.2 at 740 d, respectively, which is apparently at odds with the simple expectation that growing dust reddening should increase the ratio, while this comparison is subject to large uncertainty since Hβ at 740 d is is only detected at the $\sim 3\sigma$ level and is noise dominated.

The optical light curve (Fig. 3) followed the radioactive ^{56}Co decay during the early tail phase ($\sim$ 100 to 200 d), while thereafter ($\gtrsim$ 200 d) it was dimmer than the initial ^{56}Co tail, and faded at a faster rate of $\approx$ 1.3 mag (100 d)$^{-1}$between $\sim 300-500$ d. Similar light-curve evolution was seen for SN 2004dj, which had strong evidence of dust formation. On the other hand, the flattening of the very late time (>500 d) light curves of ASASSN-16at (as mentioned in §3) do not fit well with the proposed dust formation. Although the exact source of the flattening is unclear, it may be explained by additional flux from light echo or from the onset of a weak ejecta-CSM interaction. Such flattening at very late times was observed in SN 2007od (Inserra et al. 2011). Another unusual aspect of ASASSN-16at is weak emission lines in the late-nebular spectra, especially for [O I] ($\lambda\lambda$6300, 6364), which is one of the strongest nebular emission features for SNe with massive progenitors like SNe II. In some SNe IIn we observe such missing nebular features as the dense CSM obscures most of the emission from the SN. This does not seem to be the case for ASASSN-16at, as we do not see any evidence for dense CSM during its entire evolution, which is discussed further below. One possibility is that the dust diminishes most emission lines from the SN, while only the strongest H I and Ca II emissions remain detectable.

The asymmetry of H I emission lines is sometimes attributed to CSM interaction since CSM distributions can be sculpted to produce asymmetric line profiles as the ejecta interacts with the CSM. For instance, a triple-component profile was seen in the SN IIL/n 1996al, which was attributed to interaction with a highly asymmetric CSM (Benetti et al. 2016) or multiple peaks seen in the strongly interacting SN IIL/n 1998S (Pozzo et al. 2004; Fransson et al. 2005). But in these cases there is always a nebular emission component in the rest position, which is associated with the SN ejecta itself (see Fig. 4). Interacting SNe with no asymmetry in the inner regions should always show an emission component near zero velocity, which is from the symmetric inner region. Furthermore, for the interacting SNe in our compari-

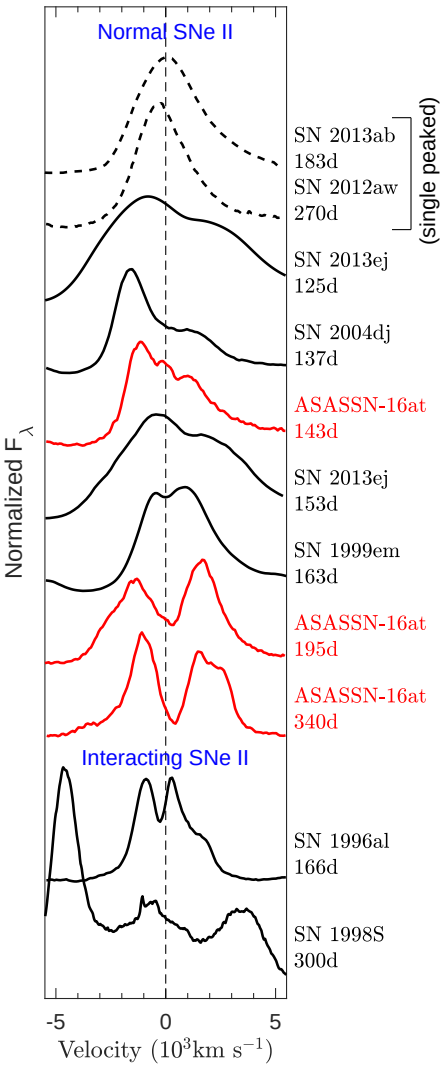

Figure 4. The double peaked Hα profile of ASASSN-16at as compared to both interacting type II SNe as well as normal SNe IIP/L having asymmetry in inner ejecta. For comparison, SNe 2012aw (Bose et al. 2013) and 2013ab (Bose et al. 2015a) are also shown as typical of the majority of normal type IIP/L SNe, which have symmetric, single component line profiles, indicating a symmetrical inner ejecta. SNe 2013ej (Bose et al. 2015b, 153d spectrum from WISeREP), 2004dj (Vinkó et al. 2006) and 1999em (Leonard et al. 2002) are also normal type IIP/L SNe but show asymmetric nebular phase spectra due to asymmetry in the ^{56}Ni distribution or the inner line forming region. On the other hand, SNe 1996al (Benetti et al. 2016) and 1998S (Pozzo et al. 2004) are type II SNe with strong ejecta-CSM interaction signatures seen in the early time, as well as nebular spectra with multi- or double- component line profiles.

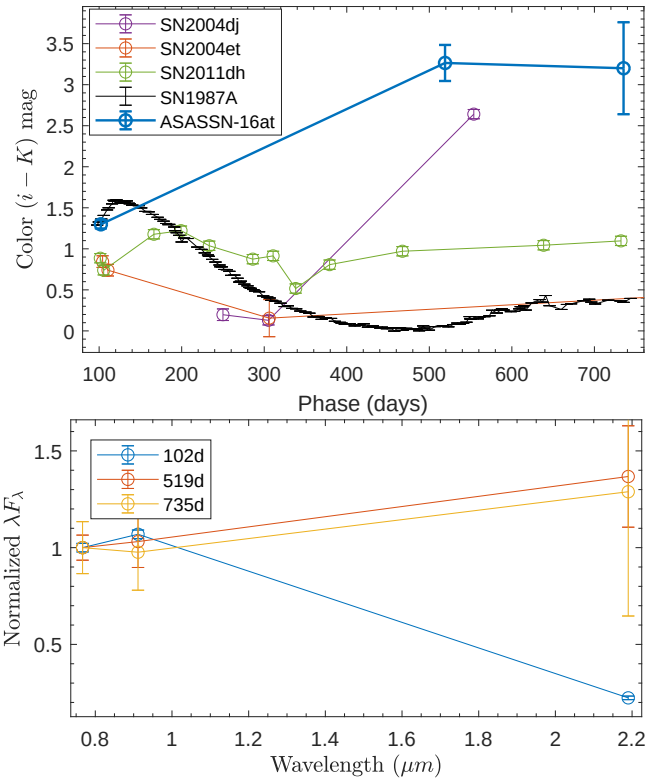

Figure 5. The top panel shows the post-photospheric phase ($i-K$) optical-to-NIR colors of ASASSN-16at as compared to other SNe II, which were also shown to have late-time dust formation with MIR observations. The red color of ASASSN-16at offers supportive evidence for late-time dust formation. The bottom panel shows the evolution of the i, z, K band SED normalized to the i-band fluxes. The change of the SED shape in later phases, peaking towards IR, also supports dust formation.

son sample, the central component also becomes more prominent as the SN evolves to deeper nebular phase. Such a component at rest is absent in the nebular H I profile for ASASSN-16at, thus we argue that CSM interaction alone cannot explain the observed double-peaked profile without a bipolar inner ejecta. In addition, the lack of IIn-like features in the early-phase spectra of ASASSN-16at suggests the absence of a dense CSM, so there is no other conceivable mechanism which can obscure the H I emission from the SN itself, as it is generally discussed in cases of SNe IIn. Furthermore, the level of X-ray emissions from ASASSN-16at is typical of normal SNe II (Dwarkadas & Gruszko 2012), suggesting that the progenitor does not have a dense CSM but rather has a typical stellar wind from a RSG star with a nominal mass loss rate of $\sim 10^{-6} - 10^{-7}$M$_\odot$ yr^{-1}. As the shock expands, the density becomes too low to produce X-rays or to radiate the X-rays fast enough to compete with adiabatic losses and eventually the X-ray emission fades.

Among the few dozen SNe IIP with nebular phase spectra in the literature (e.g., Maguire et al. 2012; Silverman et al. 2017), there is no object with distinctly double-peaked nebular Balmer lines as seen in ASASSN-

16at. Systematic studies will be needed to establish the frequency of such profiles and their correlation with other SN properties. ASASSN-16at demonstrates the importance of late-time observations for SNe II, even for those with rather "normal" properties shown during the photospheric phase.

We thank Juna A. Kollmeier who enabled our Magellan observations of this target during her program. We thank Andrea Pastorello for help in acquiring observational data and Eran Ofek and Boaz Katz for useful discussions. We thank Belinda Wilkes, late Neil Gehrels, and the *Swift* team for *Chandra* DDT and *Swift* ToO requests. We acknowledge the SN spectral repository WISeREP (http://wiserep.weizmann.ac.il). SB, SD, and PC acknowledge NSFC Project 11573003. SB is partially supported by China postdoctoral science foundation grant No. 2018T110006. MS is supported in part by a grant (13261) from VILLUM FONDEN. D.G. acknowledges support by SAO grant #DD6-17079X. This paper is also partially based on observations collected at INAF Copernico 1.82m telescope; Galileo 1.22m telescope of the University of Padova; SB, LT are partially supported by the PRIN-INAF 2016 with the project "Toward the SKA and CTA era: discovery, localisation, and physics of transient sources". TAT is partially supported by a Simons Foundation Fellowship and an IBM Einstein Fellowship from the Institute for Advanced Study, Princeton. N.E.R. acknowledges support from the Spanish MICINN grant ESP2017-82674-R and FEDER funds. C.G. appreciates the Carlsberg Foundation funding. MG is supported by the Polish National Science Centre grant OPUS 2015/17/B/ST9/03167. This research uses data obtained through TAP. Partly based on observations made with GTC, installed in the Spanish Observatorio del Roque de los Muchachos of the Instituto de Astrofisica de Canarias (IAC). NUTS is funded in part by the Instrument center for Danish Astrophysics (IDA). ASAS-SN is supported by the Gordon and Betty Moore Foundation through grant GBMF5490 to OSU and NSF grant AST-1515927. Development of ASAS-SN has been supported by NSF grant AST-0908816, the Mt. Cuba Astronomical Foundation, CCAPP at OSU, CAS-SACA, the Villum Foundation, and George Skestos. Partly based on observations made with the NOT, operated by the Nordic Optical Telescope Scientific Association at the Observatorio del Roque de los Muchachos, La Palma, Spain, of IAC. The data presented here were obtained [in part] with ALFOSC, which is provided by the Instituto de Astrofisica de Andalucia (IAA) under a joint agreement with the University of Copenhagen and NOTSA.

REFERENCES

Benetti, S., Chugai, N. N., Utrobin, V. P., et al. 2016, MNRAS, 456, 3296

Bock, G., Shappee, B. J., Stanek, K. Z., et al. 2016, The Astronomer's Telegram, 8566

Bose, S., Kumar, B., Sutaria, F., et al. 2013, MNRAS, 433, 1871

Bose, S., Valenti, S., Misra, K., et al. 2015a, MNRAS, 450, 2373

Bose, S., Sutaria, F., Kumar, B., et al. 2015b, ApJ, 806, 160

Bouchet, P., & Danziger, I. J. 1993, A&A, 273, 451

Breeveld, A. A., Landsman, W., Holland, S. T., et al. 2011, in American Institute of Physics Conference Series, Vol. 1358, American Institute of Physics Conference Series, ed. J. E. McEnery, J. L. Racusin, & N. Gehrels, 373–376

Chambers, K. C., Magnier, E. A., Metcalfe, N., et al. 2016, ArXiv e-prints, arXiv:1612.05560

Chugai, N. N. 2006, Astronomy Letters, 32, 739

Chugai, N. N. 2007, in American Institute of Physics Conference Series, Vol. 937, Supernova 1987A: 20 Years After: Supernovae and Gamma-Ray Bursters, ed. S. Immler, K. Weiler, & R. McCray, 357–364

Chugai, N. N., Fabrika, S. N., Sholukhova, O. N., et al. 2005, Astronomy Letters, 31, 792

Dwarkadas, V. V., & Gruszko, J. 2012, MNRAS, 419, 1515

Elmhamdi, A., Danziger, I. J., Chugai, N., et al. 2003, MNRAS, 338, 939

Ergon, M., Jerkstrand, A., Sollerman, J., et al. 2015, A&A, 580, A142

Fransson, C., Challis, P. M., Chevalier, R. A., et al. 2005, ApJ, 622, 991

Gall, C., Hjorth, J., & Andersen, A. C. 2011, A&A Rev., 19, 43

Grupe, D., Dong, S., Shappee, B. J., et al. 2016, The Astronomer's Telegram, 8588

Henden, A. A., Templeton, M., Terrell, D., et al. 2016, VizieR Online Data Catalog, 2336

Holoien, T. W.-S., Brown, J. S., Stanek, K. Z., et al. 2017, MNRAS, 471, 4966

Huang, F., Wang, X.-F., Hosseinzadeh, G., et al. 2018, MNRAS, 475, 3959

Inserra, C., Turatto, M., Pastorello, A., et al. 2011, MNRAS, 417, 261

Janka, H.-T. 2012, Annual Review of Nuclear and Particle Science, 62, 407

Kalberla, P. M. W., Burton, W. B., Hartmann, D., et al. 2005, A&A, 440, 775

Khokhlov, A. M., Höflich, P. A., Oran, E. S., et al. 1999, ApJL, 524, L107

Kotak, R., Meikle, W. P. S., Farrah, D., et al. 2009, ApJ, 704, 306

Kushnir, D., & Katz, B. 2015, ApJ, 811, 97

Leonard, D. C., Filippenko, A. V., Gates, E. L., et al. 2002, PASP, 114, 35

Maeda, K., Nozawa, T., Sahu, D. K., et al. 2013, ApJ, 776, 5

Maguire, K., Di Carlo, E., Smartt, S. J., et al. 2010, MNRAS, 404, 981

Maguire, K., Jerkstrand, A., Smartt, S. J., et al. 2012, MNRAS, 420, 3451

Mattila, S., Meikle, W. P. S., Lundqvist, P., et al. 2008, MNRAS, 389, 141

Meikle, W. P. S., Kotak, R., Farrah, D., et al. 2011, ApJ, 732, 109

Pejcha, O., & Thompson, T. A. 2015, ApJ, 801, 90

Piran, T., Nakar, E., Mazzali, P., & Pian, E. 2017, ArXiv e-prints, arXiv:1704.08298

Pooley, D., Lewin, W. H. G., Fox, D. W., et al. 2002, ApJ, 572, 932

Pozzo, M., Meikle, W. P. S., Fassia, A., et al. 2004, MNRAS, 352, 457

Schlafly, E. F., & Finkbeiner, D. P. 2011, ApJ, 737, 103

Shappee, B. J., Prieto, J. L., Grupe, D., et al. 2014, ApJ, 788, 48

Shigeyama, T., & Nomoto, K. 1990, ApJ, 360, 242

Silverman, J. M., Pickett, S., Wheeler, J. C., et al. 2017, MNRAS, 467, 369

Skrutskie, M. F., Cutri, R. M., Stiening, R., et al. 2006, AJ, 131, 1163

Soker, N. 2018, ArXiv e-prints, arXiv:1810.09074

Sorce, J. G., Tully, R. B., Courtois, H. M., et al. 2014, MNRAS, 444, 527

Stritzinger, M., Taddia, F., Fransson, C., et al. 2012, ApJ, 756, 173

Sugerman, B. E. K., Ercolano, B., Barlow, M. J., et al. 2006, Science, 313, 196

Tomasella, L., Cappellaro, E., Fraser, M., et al. 2013, MNRAS, 434, 1636

Utrobin, V. P., & Chugai, N. N. 2017, MNRAS, 472, 5004

Utrobin, V. P., Chugai, N. N., & Andronova, A. A. 1995, A&A, 295, 129

Vinkó, J., Takáts, K., Sárneczky, K., et al. 2006, MNRAS, 369, 1780

Wang, L., & Wheeler, J. C. 2008, ARA&A, 46, 433

Table 1. Parameters estimated for the double-peaked profile of Hα and Hβ for the nebular spectra.

Phase[a] (days)	Line	Peak Intensity Ratio (blue/red)	Blue component (10^3 km s^{-1}) Peak shift	FWHM	Red component (10^3 km s^{-1}) Peak shift	FWHM
195.1	$H\alpha$	0.79	−1.44	2.37	1.69	1.83
	$H\beta$	0.64	−1.46	1.89	1.81	1.45
340.4	$H\alpha$	1.24	−1.06	1.51	1.65	1.72
471.1	$H\alpha$	2.83	−1.14	1.40	1.51	1.61
740.3	$H\alpha$	$\gtrsim 20$	−0.64	1.24	—	—
	$H\beta$	$\gtrsim 3$	−0.56	0.74	—	—

[a]With reference to the explosion epoch JD 2457406.42.
The measured shifts and FWHMs are in units of velocity (10^3 km s^{-1}) and are estimated by fitting two Gaussian profiles simultaneously.
The parameters for Hβ are given only when they were detectable in spectra.

APPENDIX

A. ANALYSIS OF DOUBLE-PEAKED LINE PROFILES

The Table 1 lists the parameters estimated for each component of the double-peaked nebular emission for Hα and Hβ. We estimated the ratio of peak flux for the blue to the red component for each of the emissions. The FWHM and the shifts (from the rest position) for each of the red and blue components were measured by simultaneously fitting two Gaussian profiles after subtracting a local pseudo-continuum. At 340.4d the red component of the Hα emission is irregular in shape and does not represent a Gaussian profile, so the shift is estimated by directly measuring the maximum of the emission peak. For 740.3 d only blue components for both Hα and Hβ are visible, while red components are not detectable to the limits of signal-to-noise-ratio of the spectrum. Therefore, the ratio of peak intensity is given as a rough upper limit by considering the noise from the immediate continuum of the visible emissions.

B. OBSERVING INSTRUMENTS AND DATA

B.1. *Photometry and Spectroscopy*

Photometric observations were obtained using the ASAS-SN quadruple 14cm "Brutus" telescopes, the 2.0m Liverpool telescope (LT), the Las Cumbres Observatory 1.0m telescope network and the 2.6m Nordic Optical Telescope (NOT). Spectroscopic observations were done using the ALFOSC the 2.6m NOT, the B&C spectrograph on the 1.2m Galileo Telescope, the AFOSC spectrograph on the 1.8m Copernico telescope in Asiago (Italy), the SPRAT spectrograph mounted on Liverpool Telescope, the B&C Spectrograph on the 2.5m Irenée du Pont, LDSS on the 6.5m Magellan Baade telescope, LRS on the 3.6m Telescopio Nazionale Galileo (TNG) and the OSIRIS spectrograph on 10.4m Gran Telescopio Canarias (GTC).

Optical and near infrared photometric images were reduced using standard `IRAF` tasks and PSF photometry was performed using the DAOPHOT package. The PSF radius and sky region were adjusted according to the FWHM of each image. Photometric calibrations were done using catalogs of standard stars available in the SN field. The APASS (DR9; Henden et al. 2016) catalog was used for calibrating the B and V band data, SDSS standards were used for the u, g, r, i and z band data, and the 2MASS (Skrutskie et al. 2006) catalog was used for calibrating K-band data. No template subtraction has been done for the optical bands, as the SN is still detectable in our latest observations. For K band, the host galaxy contribution is subtracted using a template observed with NOTCam at 1127 d when the SN was no longer detectable. The Swift/UVOT photometry was measured with the UVOTSOURCE task in the Heasoft package using 5" apertures and placed in the Vega magnitude system, adopting the revised zero points and sensitivity from Breeveld et al. (2011). UVOT template images were also obtained on 2017-01-10, which are used to subtract the host contamination from SN observations. The photometric data of ASASSN-16at are reported in Table 2.

Spectroscopic data were reduced and calibrated using standard procedures of `IRAF` including cosmic-ray removals. Observations of appropriate spectrophotometric standard stars were used to flux-calibrate the spectra. The ALFOSC

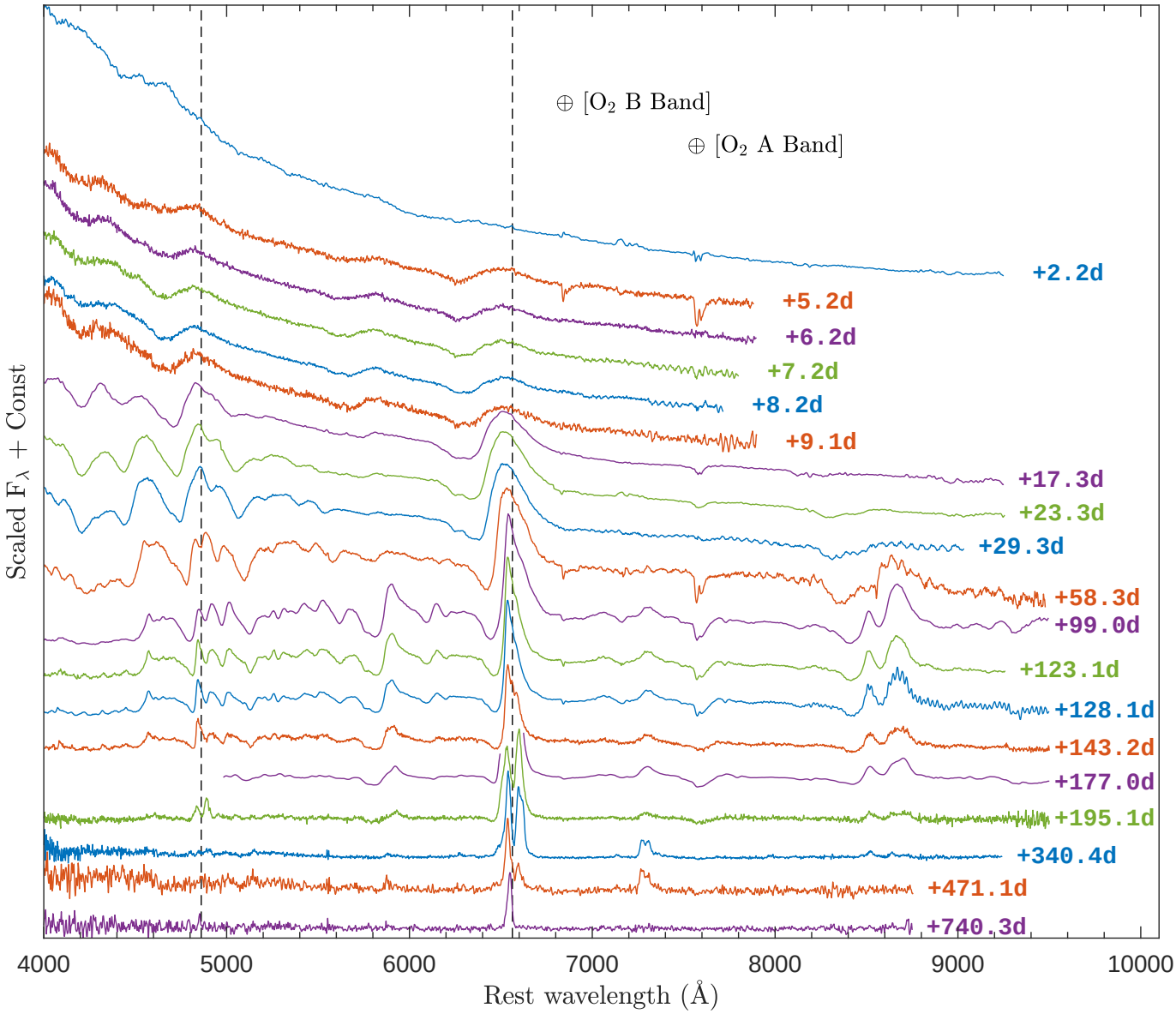

Figure 6. Spectral evolution of ASASSN-16at from 2d to 740d. The vertical dashed lines are shown to mark the rest positions of Hα and Hβ. The peak of the Hα is saturated in the spectrum observed with GTC/OSIRIS on 177.0d.

and AFOSC data were reduced using ALFOSCGUI[1]. The log of spectroscopic observations is given in Table 3. Only late-nebular spectra are shown in Fig. 1, while the full spectral sequence is shown in Fig. 6. The GTC spectrum on 2016-07-13.89 (177d) has saturation in the Hα region, and so the emission peak is clipped in the figure.

B.2. *X-ray*

Fig. 7 shows the 0.3-10 keV X-ray light curve of ASASSN-16at. The first three data points were derived from the *Swift* observations while the last one was obtained from the *Chandra* observation on UT 2016-02-06. The *Swift* X-ray telescope (XRT) was operating in photon counting mode and the data were reduced by the task *xrtpipeline* version 0.13.1., which is included in the HEASOFT package 6.16. Source counts were selected in a circle with a radius of 25″ (10 pixels). The background counts were collected in a nearby circular region with a radius of 247.″5. Due to the small number of counts used in the spectra, the counts were not binned and analyzed by applying Cash statistics.

[1] Developed by E. Cappellaro; http://sngroup.oapd.inaf.it/foscgui.html

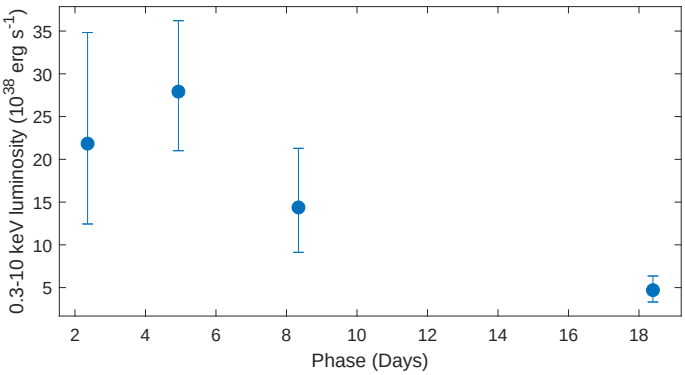

Figure 7. 0.3-10 keV X-ray luminosities of ASASSN-16at. The first three detections are from the *Swift* observations and while the last one is from *Chandra*.

The *Swift* fluxes were converted from count rates using *WPIMMS* by assuming the power law models derived from the combined *Swift* data as described below. The first data point was derived from the combined data of the first day of *Swift* observations (2016-January 21), the second from January 22 - 25, and the last *Swift* point from the observations on January-17.

After we detected ASASSN-16at in X-rays with *Swift* (Grupe et al. 2016), we submitted a short Director's Discretionary Time request of 5ks for *Chandra* which was approved and executed on 2016-February-06 06:38 for a total of 4963s. Source counts were collected in a circular region with a radius of $1^{''}$. Background counts were collected in a nearby source-free circular region with a radius of $10^{''}$. Source and background counts were collected in the $0.5-10$ keV band.

The supernova was clearly detected in X-rays by *Chandra* at a position of RA-2000 = 12:55:15.491±0.91$^{''}$ and Dec-2000 = +00:05:59.63±0.42$^{''}$. This position coincides with the optical counterpart for ASASSN-16at. A total of 5 counts were detected. This results in a background corrected count rate of 1×10^{-3} counts s^{-1} which is equivalent to a flux in the 0.3-10 keV band of $1.7^{+0.5}_{-0.6}10^{-14}$ erg s^{-1}cm^{-2}, assuming the power law spectrum with Γ=1.08 as derived from the *Swift* data (below).

C. X-RAY SPECTRAL ANALYSIS

Although the number of counts from the *Swift* observations is low it still allows some limited spectral analysis. As a first step we looked at the hardness ratios that coincided with the detections shown in Figure 7. We applied a Bayesian method to determine the hardness ratios even with very low number statistics. The hardness ratio is defined as $HR = \frac{hard-soft}{hard+soft}$ where the soft and hard counts are in the 0.3-1.0 and 1.0-10.0 keV bands, respectively. The hardness ratios from the three detections may suggest some spectral changes. While the first data point appears to be quite hard (HR=$0.72^{+0.28}_{-0.22}$), the second data point may suggest a softening of the spectrum (HR=0.01±0.29) followed be a harder spectrum again (HR=$0.38^{+0.62}_{-0.24}$).

Although the supernova was faint in X-rays and the spectrum may have changed during the observation of the first week, the *Swift* observations of the first week (January 21-27, segments 001-012) still allow a rough spectral analysis. A total of 25 counts were collected at the source position during this time frame. The absorption column density was fixed to the Galactic value of $N_{\rm H} = 1.40 \times 10^{20}$ cm^{-2} (Kalberla et al. 2005). We first fit the spectrum with a single power law model which results in an acceptable fit (C-stat 20.3/21 degrees of freedom). The X-ray spectral slope is very flat with a photon index $\Gamma = 1.08^{+0.80}_{-0.76}$. We also fit the spectrum with a blackbody model. The blackbody temperature equivalent energy is $1.34^{+2.55}_{-0.49}$ keV. Although this model still resulted in an acceptable fit (27.3/21), it is less favorable than the power law model.

Table 2. Optical photometry of ASASSN-16at.

UT Date	JD − 2,450,000	Phase[a] (days)	B (mag)	V (mag)	u (mag)	g (mag)	r (mag)	i (mag)	z (mag)	Telescope[b] / Inst.
2016-01-19.49	7406.99	0.57	—	16.805 ± 0.260	—	—	—	—	—	ASASSN
2016-01-20.59	7408.09	1.67	—	15.100 ± 0.040	—	—	—	—	—	ASASSN
2016-01-20.75	7408.25	1.83	15.012 ± 0.044	15.100 ± 0.043	—	—	15.177 ± 0.018	15.376 ± 0.018	—	LCOGT
2016-01-21.23	7408.73	2.31	—	15.040 ± 0.050	—	—	14.992 ± 0.027	—	—	ASASSN,LT
2016-01-21.46	7408.96	2.54	—	14.860 ± 0.050	—	—	—	—	—	ASASSN
2016-01-21.68	7409.18	2.76	14.820 ± 0.089	14.828 ± 0.069	—	—	—	15.125 ± 0.049	—	LCOGT
2016-01-22.16	7409.66	3.24	—	—	—	—	14.737 ± 0.023	—	—	LT
2016-01-22.32	7409.82	3.40	14.636 ± 0.017	14.703 ± 0.039	—	—	14.752 ± 0.012	14.933 ± 0.011	—	LCOGT
2016-01-22.39	7409.89	3.47	—	14.645 ± 0.035	—	—	—	—	—	ASASSN
2016-01-23.31	7410.81	4.39	—	14.445 ± 0.030	—	14.416 ± 0.030	14.536 ± 0.020	—	—	ASASSN,LT
2016-01-23.64	7411.14	4.72	14.451 ± 0.027	14.437 ± 0.035	—	—	14.467 ± 0.019	14.589 ± 0.011	—	LCOGT
2016-01-24.26	7411.76	5.34	—	—	14.005 ± 0.085	14.306 ± 0.033	14.361 ± 0.023	14.591 ± 0.036	14.710 ± 0.023	LT
2016-01-24.55	7412.05	5.63	—	14.285 ± 0.035	—	—	—	—	—	ASASSN
2016-01-25.10	7412.60	6.18	—	—	13.984 ± 0.116	14.229 ± 0.026	14.270 ± 0.017	14.492 ± 0.036	14.576 ± 0.034	LT
2016-01-25.36	7412.86	6.44	—	14.310 ± 0.030	—	—	—	—	—	ASASSN
2016-01-25.62	7413.12	6.70	—	14.170 ± 0.040	—	—	—	—	—	ASASSN
2016-01-25.66	7413.16	6.74	14.249 ± 0.037	14.213 ± 0.041	—	—	14.210 ± 0.018	14.393 ± 0.026	—	LCOGT
2016-01-26.14	7413.64	7.22	—	—	13.975 ± 0.068	14.164 ± 0.028	14.190 ± 0.022	14.353 ± 0.024	14.450 ± 0.017	LT
2016-01-26.37	7413.87	7.45	—	14.170 ± 0.030	—	—	—	—	—	ASASSN
2016-01-26.62	7414.12	7.70	—	14.180 ± 0.030	—	—	—	—	—	ASASSN
2016-01-27.07	7414.57	8.15	—	—	13.978 ± 0.094	14.149 ± 0.034	14.148 ± 0.025	14.311 ± 0.029	14.409 ± 0.016	LT
2016-01-27.62	7415.12	8.70	—	14.170 ± 0.030	—	—	—	—	—	ASASSN
2016-01-28.28	7415.78	9.36	—	14.139 ± 0.073	—	—	—	14.243 ± 0.015	—	LCOGT
2016-01-28.37	7415.87	9.45	—	14.160 ± 0.030	—	—	—	—	—	ASASSN
2016-01-28.61	7416.11	9.69	—	14.100 ± 0.040	—	—	—	—	—	ASASSN
2016-01-29.23	7416.73	10.31	14.267 ± 0.048	14.234 ± 0.270	—	—	14.119 ± 0.027	—	—	LCOGT
2016-01-29.68	7417.18	10.76	14.236 ± 0.017	14.128 ± 0.039	—	—	14.064 ± 0.036	14.189 ± 0.028	—	LCOGT
2016-01-30.25	7417.75	11.33	14.307 ± 0.019	14.192 ± 0.058	—	—	14.133 ± 0.022	14.220 ± 0.027	—	LCOGT
2016-01-30.61	7418.11	11.69	—	14.030 ± 0.030	—	—	—	—	—	ASASSN
2016-01-30.65	7418.15	11.73	14.272 ± 0.026	14.146 ± 0.041	—	—	14.104 ± 0.018	14.182 ± 0.024	—	LCOGT
2016-01-30.97	7418.47	12.05	14.340 ± 0.055	14.187 ± 0.045	—	—	14.143 ± 0.023	14.251 ± 0.019	—	LCOGT
2016-01-31.09	7418.59	12.17	—	—	—	—	14.141 ± 0.039	—	—	LT
2016-01-31.60	7419.10	12.68	—	14.120 ± 0.020	—	—	—	—	—	ASASSN
2016-01-31.72	7419.22	12.80	14.357 ± 0.045	14.197 ± 0.043	—	—	14.126 ± 0.023	14.213 ± 0.016	—	LCOGT
2016-02-01.47	7419.97	13.55	—	14.150 ± 0.030	—	—	—	—	—	ASASSN
2016-02-01.61	7420.11	13.69	14.421 ± 0.058	14.197 ± 0.049	—	—	14.128 ± 0.019	14.234 ± 0.028	—	LCOGT
2016-02-03.16	7421.66	15.24	—	—	—	—	14.133 ± 0.018	—	—	LT
2016-02-03.48	7421.98	15.56	—	14.225 ± 0.020	—	—	—	—	—	ASASSN
2016-02-04.12	7422.62	16.20	—	—	—	—	14.148 ± 0.022	—	—	LT
2016-02-04.33	7422.83	16.41	—	—	—	—	—	—	—	ASASSN
2016-02-05.03	7423.53	17.11	14.512 ± 0.042	14.273 ± 0.041	—	—	14.191 ± 0.018	14.287 ± 0.017	—	LCOGT
2016-02-05.16	7423.66	17.24	—	—	14.689 ± 0.068	14.344 ± 0.024	14.166 ± 0.018	14.293 ± 0.024	14.331 ± 0.013	LT
2016-02-05.57	7424.07	17.65	—	14.290 ± 0.020	—	—	—	—	—	ASASSN
2016-02-05.96	7424.46	18.04	14.610 ± 0.056	14.338 ± 0.039	—	—	14.244 ± 0.019	14.342 ± 0.041	—	LCOGT
2016-02-06.32	7424.82	18.40	—	—	—	—	—	—	—	ASASSN
2016-02-06.60	7425.10	18.68	—	14.270 ± 0.182	—	—	—	—	—	LCOGT
2016-02-07.15	7425.65	19.23	—	—	14.942 ± 0.067	14.407 ± 0.026	14.165 ± 0.012	14.297 ± 0.027	14.349 ± 0.017	LT
2016-02-07.60	7426.10	19.68	14.686 ± 0.037	14.361 ± 0.048	—	—	14.220 ± 0.018	14.302 ± 0.015	—	LCOGT
2016-02-08.23	7426.73	20.31	—	—	15.094 ± 0.067	14.420 ± 0.023	14.169 ± 0.018	14.327 ± 0.024	14.343 ± 0.014	LT
2016-02-08.68	7427.18	20.76	14.731 ± 0.046	14.354 ± 0.039	—	—	14.230 ± 0.022	14.302 ± 0.014	—	LCOGT
2016-02-09.07	7427.57	21.15	—	—	15.211 ± 0.088	14.464 ± 0.027	14.181 ± 0.021	14.367 ± 0.025	14.341 ± 0.015	LT
2016-02-09.59	7428.09	21.67	14.759 ± 0.043	14.303 ± 0.053	—	—	14.226 ± 0.025	14.325 ± 0.023	—	LCOGT
2016-02-10.25	7428.75	22.33	—	—	15.373 ± 0.066	14.483 ± 0.026	14.198 ± 0.016	14.336 ± 0.029	14.350 ± 0.018	LT
2016-02-10.62	7429.12	22.70	14.803 ± 0.031	14.376 ± 0.049	—	—	14.166 ± 0.019	14.222 ± 0.018	—	LCOGT
2016-02-11.94	7430.44	24.02	14.860 ± 0.034	14.382 ± 0.044	—	—	14.232 ± 0.022	14.333 ± 0.013	—	LCOGT
2016-02-12.04	7430.54	24.12	—	—	15.562 ± 0.118	14.560 ± 0.026	14.209 ± 0.016	14.401 ± 0.030	14.355 ± 0.023	LT
2016-02-12.63	7431.13	24.71	14.935 ± 0.038	14.470 ± 0.049	—	—	14.281 ± 0.024	14.370 ± 0.021	—	LCOGT
2016-02-13.58	7432.08	25.66	14.996 ± 0.050	14.462 ± 0.037	—	—	14.288 ± 0.018	14.388 ± 0.015	—	LCOGT
2016-02-14.19	7432.69	26.27	—	—	15.948 ± 0.075	14.645 ± 0.026	14.252 ± 0.017	14.402 ± 0.023	14.407 ± 0.023	LT
2016-02-15.06	7433.56	27.14	—	—	—	—	14.260 ± 0.017	—	—	LT
2016-02-17.05	7435.55	29.13	—	—	—	—	—	—	14.422 ± 0.016	LT
2016-02-18.07	7436.57	30.15	—	—	—	—	14.315 ± 0.017	—	—	LT
2016-02-18.76	7437.26	30.84	15.269 ± 0.035	14.606 ± 0.047	—	—	14.408 ± 0.021	14.442 ± 0.017	—	LCOGT
2016-02-20.92	7439.42	33.00	15.376 ± 0.035	14.654 ± 0.046	—	—	14.407 ± 0.020	14.467 ± 0.017	—	LCOGT

Table 2 continued

Table 2 *(continued)*

UT Date	JD − 2,450,000	Phase[a] (days)	B (mag)	V (mag)	u (mag)	g (mag)	r (mag)	i (mag)	z (mag)	Telescope[b] / Inst.
2016-02-23.92	7442.42	36.00	15.520 ± 0.037	14.744 ± 0.054	—	—	14.437 ± 0.019	14.552 ± 0.036	—	LCOGT
2016-02-26.94	7445.44	39.02	15.538 ± 0.032	14.674 ± 0.042	—	—	14.458 ± 0.022	14.558 ± 0.022	—	LCOGT
2016-02-28.64	7447.14	40.72	15.544 ± 0.031	14.714 ± 0.040	—	—	14.454 ± 0.018	14.538 ± 0.016	—	LCOGT
2016-03-01.59	7449.09	42.67	15.579 ± 0.024	14.746 ± 0.030	—	—	14.475 ± 0.027	14.558 ± 0.017	—	LCOGT
2016-03-03.61	7451.11	44.69	15.643 ± 0.031	14.805 ± 0.042	—	—	14.474 ± 0.020	14.575 ± 0.014	—	LCOGT
2016-03-04.08	7451.58	45.16	—	—	17.075 ± 0.072	15.107 ± 0.026	14.466 ± 0.016	14.557 ± 0.025	14.529 ± 0.015	LT
2016-03-05.53	7453.03	46.61	15.694 ± 0.077	14.775 ± 0.041	—	—	—	14.572 ± 0.020	—	LCOGT
2016-03-05.99	7453.49	47.07	—	—	17.135 ± 0.072	15.104 ± 0.026	14.462 ± 0.018	14.558 ± 0.026	14.517 ± 0.014	LT
2016-03-07.67	7455.17	48.75	15.697 ± 0.028	14.821 ± 0.038	—	—	14.491 ± 0.024	14.588 ± 0.015	—	LCOGT
2016-03-08.02	7455.52	49.10	—	—	17.195 ± 0.071	15.132 ± 0.025	14.460 ± 0.020	14.575 ± 0.029	14.532 ± 0.022	LT
2016-03-10.03	7457.53	51.11	—	—	17.452 ± 0.185	15.143 ± 0.025	14.511 ± 0.034	14.588 ± 0.025	14.538 ± 0.014	LT
2016-03-11.60	7459.10	52.68	15.792 ± 0.032	14.854 ± 0.035	—	—	14.532 ± 0.020	14.592 ± 0.018	—	LCOGT
2016-03-11.95	7459.45	53.03	—	—	17.327 ± 0.081	15.154 ± 0.026	14.510 ± 0.025	14.579 ± 0.027	14.533 ± 0.021	LT
2016-03-13.53	7461.03	54.61	15.839 ± 0.049	14.875 ± 0.051	—	—	14.559 ± 0.028	14.602 ± 0.022	—	LCOGT
2016-03-14.03	7461.53	55.11	—	—	17.375 ± 0.067	15.193 ± 0.025	14.516 ± 0.014	14.594 ± 0.025	14.535 ± 0.014	LT
2016-03-14.11	7461.61	55.19	15.796 ± 0.064	14.853 ± 0.037	—	—	14.537 ± 0.023	14.572 ± 0.016	—	LCOGT
2016-03-15.07	7462.57	56.15	—	—	—	—	14.562 ± 0.026	—	—	LT
2016-03-15.51	7463.01	56.59	15.801 ± 0.065	14.884 ± 0.046	—	—	14.569 ± 0.023	14.621 ± 0.020	—	LCOGT
2016-03-16.01	7463.51	57.09	—	—	17.478 ± 0.067	15.247 ± 0.025	14.533 ± 0.012	14.615 ± 0.025	14.543 ± 0.015	LT
2016-03-17.58	7465.08	58.66	15.933 ± 0.034	14.911 ± 0.047	—	—	14.585 ± 0.015	14.648 ± 0.017	—	LCOGT
2016-03-19.00	7466.50	60.08	—	—	17.623 ± 0.089	15.294 ± 0.026	14.579 ± 0.013	14.660 ± 0.024	14.608 ± 0.019	LT
2016-03-19.85	7467.35	60.93	16.045 ± 0.060	—	—	—	—	14.660 ± 0.033	—	LCOGT
2016-03-21.51	7469.01	62.59	—	14.988 ± 0.055	—	—	14.661 ± 0.035	14.684 ± 0.032	—	LCOGT
2016-03-23.84	7471.34	64.92	15.997 ± 0.205	15.078 ± 0.182	—	—	14.725 ± 0.083	14.777 ± 0.119	—	LCOGT
2016-03-25.55	7473.05	66.63	16.196 ± 0.115	15.003 ± 0.079	—	—	14.690 ± 0.023	14.710 ± 0.041	—	LCOGT
2016-03-27.07	7474.57	68.15	—	—	17.998 ± 0.069	15.454 ± 0.025	14.694 ± 0.014	14.751 ± 0.023	14.632 ± 0.017	LT
2016-03-27.85	7475.35	68.93	16.249 ± 0.269	15.084 ± 0.065	—	—	14.779 ± 0.051	14.738 ± 0.037	—	LCOGT
2016-03-28.07	7475.57	69.15	—	—	—	—	14.707 ± 0.015	—	—	LT
2016-03-28.97	7476.47	70.05	—	—	—	—	14.720 ± 0.020	—	—	LT
2016-03-30.85	7478.35	71.93	16.326 ± 0.044	15.121 ± 0.047	—	—	14.800 ± 0.018	14.797 ± 0.025	—	LCOGT
2016-03-31.96	7479.46	73.04	—	—	—	—	14.746 ± 0.023	—	—	LT
2016-04-03.08	7481.58	75.16	16.366 ± 0.041	15.180 ± 0.050	—	—	14.843 ± 0.017	14.829 ± 0.024	—	LCOGT
2016-04-05.50	7484.00	77.58	16.369 ± 0.037	15.203 ± 0.048	—	—	14.843 ± 0.018	14.877 ± 0.022	—	LCOGT
2016-04-05.98	7484.48	78.06	—	—	—	—	14.818 ± 0.024	—	—	LT
2016-04-08.54	7487.04	80.62	16.565 ± 0.060	15.266 ± 0.040	—	—	14.900 ± 0.021	14.894 ± 0.023	—	LCOGT
2016-04-10.95	7489.45	83.03	—	—	—	—	14.919 ± 0.016	—	—	LT
2016-04-11.50	7490.00	83.58	16.569 ± 0.047	15.335 ± 0.049	—	—	14.941 ± 0.024	14.912 ± 0.027	—	LCOGT
2016-04-14.08	7492.58	86.16	—	—	18.988 ± 0.073	15.893 ± 0.025	14.989 ± 0.018	14.997 ± 0.026	14.886 ± 0.014	LT
2016-04-14.50	7493.00	86.58	—	15.428 ± 0.039	—	—	—	—	—	LCOGT
2016-04-18.47	7496.97	90.55	17.089 ± 0.071	15.577 ± 0.045	—	—	15.168 ± 0.028	15.117 ± 0.021	—	LCOGT
2016-04-20.51	7499.01	92.59	16.753 ± 0.252	15.684 ± 0.147	—	—	—	15.302 ± 0.169	—	LCOGT
2016-04-23.16	7501.66	95.24	—	—	—	16.561 ± 0.039	15.584 ± 0.039	15.532 ± 0.028	15.362 ± 0.025	LT
2016-04-24.39	7502.89	96.47	17.837 ± 0.144	16.315 ± 0.052	—	—	15.798 ± 0.043	—	—	LCOGT
2016-04-25.43	7503.93	97.51	18.042 ± 0.067	16.506 ± 0.044	—	—	15.996 ± 0.021	15.968 ± 0.018	—	LCOGT
2016-04-26.10	7504.60	98.18	—	—	20.313 ± 0.159	17.164 ± 0.028	16.026 ± 0.017	16.062 ± 0.027	15.800 ± 0.019	LT
2016-04-26.75	7505.25	98.83	18.180 ± 0.068	16.649 ± 0.031	—	—	16.119 ± 0.014	16.108 ± 0.022	—	LCOGT
2016-05-07.96	7516.46	110.04	—	—	—	17.349 ± 0.038	16.324 ± 0.031	16.347 ± 0.029	16.110 ± 0.029	LT
2016-05-09.85	7518.35	111.93	18.309 ± 0.067	16.885 ± 0.048	—	—	—	—	—	LCOGT
2016-05-10.78	7519.28	112.86	18.477 ± 0.039	16.924 ± 0.034	—	—	16.436 ± 0.021	—	—	LCOGT
2016-05-11.85	7520.35	113.93	18.438 ± 0.046	16.992 ± 0.042	—	—	—	—	—	LCOGT
2016-05-14.91	7523.41	116.99	—	—	—	17.504 ± 0.028	16.457 ± 0.017	16.447 ± 0.024	16.211 ± 0.016	LT
2016-05-16.76	7525.26	118.84	18.626 ± 0.105	17.058 ± 0.058	—	—	16.477 ± 0.021	16.427 ± 0.037	—	LCOGT
2016-05-17.98	7526.48	120.06	18.468 ± 0.574	—	—	—	16.401 ± 0.103	16.506 ± 0.243	—	LCOGT
2016-05-20.78	7529.28	122.86	18.414 ± 0.068	16.951 ± 0.050	—	—	16.452 ± 0.015	16.452 ± 0.037	—	LCOGT
2016-05-20.99	7529.49	123.07	—	—	20.829 ± 0.221	17.443 ± 0.030	16.447 ± 0.013	16.460 ± 0.025	16.167 ± 0.014	LT
2016-05-23.94	7532.44	126.02	—	—	—	17.557 ± 0.027	16.558 ± 0.018	16.593 ± 0.026	16.286 ± 0.017	LT
2016-05-24.38	7532.88	126.46	18.422 ± 0.080	17.079 ± 0.043	—	—	16.607 ± 0.021	16.564 ± 0.027	—	LCOGT
2016-05-25.88	7534.38	127.96	—	—	—	—	16.594 ± 0.018	—	—	LT
2016-05-29.77	7538.27	131.85	18.551 ± 0.053	17.269 ± 0.044	—	—	—	16.639 ± 0.026	—	LCOGT
2016-05-30.89	7539.39	132.97	—	—	—	—	16.680 ± 0.017	—	—	LT
2016-06-29.09	7568.59	162.17	18.692 ± 0.041	17.628 ± 0.035	—	—	16.911 ± 0.017	16.958 ± 0.021	—	LCOGT
2016-07-14.41	7583.91	177.49	18.427 ± 0.177	—	—	—	—	—	—	LCOGT
2016-07-19.80	7589.30	182.88	18.797 ± 1.278	—	—	—	—	—	—	LCOGT
2016-08-07.72	7608.22	201.80	—	19.087 ± 1.727	—	—	17.515 ± 0.221	18.447 ± 0.622	—	LCOGT

Table 2 continued

Table 2 *(continued)*

UT Date	JD − 2,450,000	Phase[a] (days)	B (mag)	V (mag)	u (mag)	g (mag)	r (mag)	i (mag)	z (mag)	Telescope[b] / Inst.
2016-11-16.27	7708.77	302.35	—	—	—	19.947 ± 0.239	19.210 ± 0.112	19.865 ± 0.265	19.967 ± 0.384	LT
2016-12-10.26	7732.76	326.34	—	—	—	20.833 ± 0.040	19.662 ± 0.028	20.235 ± 0.039	20.079 ± 0.061	LT
2016-12-30.17	7752.67	346.25	—	—	—	20.211 ± 0.420	19.974 ± 0.157	20.504 ± 0.108	20.421 ± 0.469	LT
2017-03-01.15	7813.65	407.23	—	—	—	21.436 ± 0.044	20.732 ± 0.036	20.915 ± 0.072	21.071 ± 0.101	LT
2017-03-05.04	7817.54	411.12	—	—	—	—	20.622 ± 0.050	20.893 ± 0.060	—	LT
2017-03-08.11	7820.61	414.19	—	—	—	—	20.793 ± 0.051	21.143 ± 0.069	—	LT
2017-03-08.97	7821.47	415.05	—	—	—	21.114 ± 0.096	—	—	—	LT
2017-03-10.00	7822.50	416.08	—	—	—	—	20.785 ± 0.139	20.734 ± 0.143	—	LT
2017-04-03.08	7846.58	440.16	—	—	—	21.510 ± 0.052	20.953 ± 0.046	21.160 ± 0.065	—	LT
2017-04-05.95	7849.45	443.03	—	—	—	—	21.195 ± 0.061	21.453 ± 0.073	—	LT
2017-04-07.93	7851.43	445.01	—	—	—	—	21.161 ± 0.120	21.171 ± 0.104	—	LT
2017-04-12.99	7856.49	450.07	—	—	—	21.787 ± 0.135	—	—	—	LT
2017-04-16.99	7860.49	454.07	—	—	—	—	21.330 ± 0.040	21.465 ± 0.046	—	LT
2018-01-10.25	8128.75	722.33	—	—	—	—	21.563 ± 0.067	—	—	LT
2018-01-11.22	8129.72	723.30	—	—	—	—	—	—	22.008 ± 0.214	LT
2018-01-19.28	8137.78	731.36	—	—	—	—	—	22.206 ± 0.150	—	LT
2018-01-25.24	8143.74	737.32	—	—	—	22.034 ± 0.047	—	—	—	LT
2018-03-13.06	8190.56	784.14	—	—	—	—	—	22.397 ± 0.094	—	LT
2018-05-11.90	8250.40	843.98	—	—	—	—	21.774 ± 0.038	—	—	LT
2018-06-17.89	8287.39	880.97	—	—	—	—	—	22.655 ± 0.113	—	LT

Table 2. *(continued)* NIR photometry.

UT Date	JD − 2,450,000	Phase[a] (days)	K (mag)	Telescope[b] / Inst.
2016-04-30.02	7508.52	102.10	14.85 ± 0.05	NC
2017-06-20.97	7925.47	519.05	18.34 ± 0.21	NC
2018-01-23.23	8141.73	735.31	18.99 ± 0.54	NC
2019-02-19.12	8533.62	1127.20	—	NC

Table 2. *(continued)* NUV photometry.

UT Date	JD − 2,450,000	Phase[a] (days)	uvw2 (mag)	uvm2 (mag)	uvw1 (mag)	uvu (mag)	uvb (mag)	uvv (mag)	Telescope[b] / Inst.
2016-01-21.08	7408.58	2.16	12.742 ± 0.038	12.718 ± 0.039	12.899 ± 0.037	13.479 ± 0.033	14.829 ± 0.033	14.822 ± 0.045	UVOT
2016-01-21.51	7409.01	2.59	13.030 ± 0.038	12.886 ± 0.038	12.930 ± 0.038	13.413 ± 0.035	14.741 ± 0.035	14.803 ± 0.045	UVOT
2016-01-22.45	7409.95	3.53	12.891 ± 0.038	12.745 ± 0.039	12.871 ± 0.038	13.254 ± 0.035	14.550 ± 0.035	14.673 ± 0.045	UVOT
2016-01-22.79	7410.29	3.87	12.815 ± 0.039	12.686 ± 0.038	12.826 ± 0.038	13.202 ± 0.034	14.496 ± 0.033	14.516 ± 0.039	UVOT
2016-01-23.19	7410.69	4.27	12.789 ± 0.039	12.625 ± 0.039	12.730 ± 0.039	13.118 ± 0.038	14.366 ± 0.038	14.474 ± 0.051	UVOT
2016-01-23.66	7411.16	4.74	—	—	12.700 ± 0.046	—	—	—	UVOT
2016-01-24.79	7412.29	5.87	13.037 ± 0.037	12.757 ± 0.038	12.743 ± 0.037	12.964 ± 0.033	14.234 ± 0.031	14.217 ± 0.032	UVOT
2016-01-25.26	7412.76	6.34	13.156 ± 0.040	12.835 ± 0.040	12.884 ± 0.041	13.032 ± 0.041	14.247 ± 0.042	14.184 ± 0.054	UVOT
2016-01-27.17	7414.67	8.25	13.546 ± 0.039	13.237 ± 0.039	—	—	—	—	UVOT
2016-02-01.03	7419.53	13.11	14.568 ± 0.041	—	13.868 ± 0.040	13.275 ± 0.035	14.293 ± 0.033	14.133 ± 0.038	UVOT
2016-02-01.76	7420.26	13.84	14.760 ± 0.041	—	14.029 ± 0.040	13.363 ± 0.035	14.298 ± 0.033	14.178 ± 0.038	UVOT
2016-02-06.69	7425.19	18.77	15.959 ± 0.159	—	15.209 ± 0.056	14.049 ± 0.043	14.488 ± 0.040	—	UVOT
2016-02-07.05	7425.55	19.13	16.177 ± 0.053	16.323 ± 0.059	15.244 ± 0.046	14.058 ± 0.036	14.535 ± 0.033	14.287 ± 0.039	UVOT
2016-02-08.60	7427.10	20.68	16.527 ± 0.069	16.797 ± 0.086	15.627 ± 0.058	14.251 ± 0.042	14.691 ± 0.038	14.310 ± 0.043	UVOT
2016-02-09.93	7428.43	22.01	16.841 ± 0.065	17.076 ± 0.077	15.858 ± 0.054	14.553 ± 0.039	14.683 ± 0.034	14.275 ± 0.036	UVOT
2016-02-10.39	7428.89	22.47	16.876 ± 0.081	17.125 ± 0.094	15.894 ± 0.065	14.547 ± 0.045	14.718 ± 0.039	14.356 ± 0.045	UVOT
2016-02-17.44	7435.94	29.52	18.064 ± 0.164	—	16.981 ± 0.090	15.491 ± 0.052	15.151 ± 0.038	—	UVOT
2016-02-17.92	7436.42	30.00	—	18.569 ± 0.249	—	—	—	14.481 ± 0.052	UVOT
2016-02-20.56	7439.06	32.64	18.286 ± 0.209	19.070 ± 0.363	17.533 ± 0.172	15.628 ± 0.075	15.228 ± 0.050	14.615 ± 0.059	UVOT
2016-02-21.57	7440.07	33.65	18.575 ± 0.170	19.438 ± 0.370	17.232 ± 0.094	15.785 ± 0.052	15.248 ± 0.036	14.580 ± 0.038	UVOT
2016-02-23.58	7442.08	35.66	18.387 ± 0.181	18.910 ± 0.268	17.416 ± 0.105	16.042 ± 0.059	15.348 ± 0.037	14.652 ± 0.049	UVOT
2016-03-01.60	7449.10	42.68	18.601 ± 0.205	—	17.733 ± 0.152	16.253 ± 0.077	15.518 ± 0.044	14.746 ± 0.048	UVOT
2016-03-05.33	7452.83	46.41	18.868 ± 0.218	—	17.771 ± 0.136	16.318 ± 0.069	15.607 ± 0.041	14.762 ± 0.042	UVOT

NOTE—
[a] With reference to the explosion epoch JD 2457406.42.
[b] The abbreviations of telescope/instrument used are as follows: ASASSN - ASAS-SN quadruple 14-cm telescopes; LCOGT - Las Cumbres Observatory 1 m telescope network; LT - 2m Liverpool Telescope; NC - NOTCam mounted on 2.0m NOT; UVOT - *Swift* Ultraviolet Optical Telescope.
Data observed within 5 hr are represented under a single-epoch observation.

Table 3. Summary of spectroscopic observations of ASASSN-16at.

UT Date	JD 2450000+	Phase[a] (days)	Telescope / Instrument
2016-01-21.11	7408.61	2.2	Copernico/AFOSC
2016-01-24.14	7411.64	5.2	Galileo/B&C
2016-01-25.16	7412.66	6.2	Galileo/B&C
2016-01-26.13	7413.63	7.2	Galileo/B&C
2016-01-27.08	7414.58	8.2	Galileo/B&C
2016-01-28.06	7415.56	9.1	Galileo/B&C
2016-02-05.24	7423.74	17.3	Copernico/AFOSC
2016-02-11.17	7429.67	23.3	NOT/ALFOSC
2016-02-17.20	7435.70	29.3	NOT/ALFOSC
2016-03-17.20	7464.70	58.3	DuPont/B&C
2016-04-26.92	7505.42	99.0	NOT/ALFOSC
2016-05-20.99	7529.49	123.1	NOT/ALFOSC
2016-05-26.00	7534.50	128.1	TNG/LRS
2016-06-10.13	7549.63	143.2	DuPont/B&C
2016-07-13.89	7583.39	177.0	GTC/OSIRIS
2016-08-01.01	7601.51	195.1	DuPont/B&C
2016-12-24.34	7746.84	340.4	Magellan/LDSS3
2017-05-03.98	7877.48	471.1	GTC/OSIRIS
2018-01-28.17	8146.67	740.3	GTC/OSIRIS

[a] The phase is the number of days after the adopted explosion epoch JD 2457406.42